



Atomistic study on the microscopic mechanism of grain boundary embrittlement induced by small dense helium bubbles in iron

Lei Peng^{1,2} · Yong-Jie Sun^{1,2} · Jing-Yi Shi^{1,2} · Yi-Fei Liu^{1,2} · Shang-Ming Chen^{1,2} · Liu-Liu Li^{1,2,3}

Received: 25 July 2023 / Revised: 28 November 2023 / Accepted: 29 November 2023 / Published online: 3 May 2024

© The Author(s), under exclusive licence to China Science Publishing & Media Ltd. (Science Press), Shanghai Institute of Applied Physics, the Chinese Academy of Sciences, Chinese Nuclear Society 2024

Abstract

The helium bubbles induced by 14 MeV neutron irradiation can cause intergranular fractures in reduced activation ferritic martensitic steel, which is a candidate structural material for fusion reactors. In order to elucidate the susceptibility of different grain boundaries (GBs) to helium-induced embrittlement, the tensile fracture processes of 10 types of GBs with and without helium bubbles in body-centered cubic (bcc) iron at the relevant service temperature of 600 K were investigated via molecular dynamics methods. The results indicate that in the absence of helium bubbles, the GBs studied here can be classified into two distinct categories: brittle GBs and ductile GBs. The atomic scale analysis shows that the plastic deformation of ductile GB at high temperatures originates from complex plastic deformation mechanisms, including the Bain/Burgers path phase transition and deformation twinning, in which the Bain path phase transition is the most dominant plastic deformation mechanism. However, the presence of helium bubbles severely inhibits the plastic deformation channels of the GBs, resulting in a significant decrease in elongation at fractures. For bubble-decorated GBs, the ultimate tensile strength increases with the increase in the misorientation angle. Interestingly, the coherent twin boundary $\Sigma 3\{112\}$ was found to maintain relatively high fracture strength and maximum failure strain under the influence of helium bubbles.

Keywords Helium bubble · Grain boundary · Embrittlement · Reduced activation ferritic martensitic steel · Molecular dynamics · Bain path

This work was supported by the National Natural Science Foundation of China (Nos. 12175231 and 11805131), Anhui Natural Science Foundation of China (No. 2108085J05), the National Key Research and Development Plan of China (No. 2018YFE0307101), and the Collaborative Innovation Program of the Hefei Science Center, CAS (Nos. 2021HSC-CIP020 and 2022HSC-CIP009).

✉ Jing-Yi Shi
shijy@ustc.edu.cn

¹ State Key Laboratory of Particle Detection and Electronics, University of Science and Technology of China, Hefei 230026, China

² School of Nuclear Science and Technology, University of Science and Technology of China, Hefei 230027, China

³ Science and Technology on Reactor System Design Technology Laboratory, Nuclear Power Institute of China, Chengdu 610213, China

1 Introduction

Reduced activation ferritic martensitic (RAFM) steel and its improved models, such as oxide dispersion strengthened (ODS), thermomechanical treatments (TMT), and castable nanostructured alloys (CNA) steels, are the primary candidate structural steels for future fusion reactor and advanced fission reactors owing to their excellent irradiation resistance, high temperature performance, and high level of technological and processing maturity [1–8]. However, in the service environment of fusion reactors, high-energy neutron irradiation will introduce a large number of helium atoms (i.e., up to 10–15 appm/dpa) into structural steel through the (n, α) reaction [9–11]. Due to the extremely low solubility of helium atoms in metallic alloys, helium atoms have a strong tendency to coalesce in the form of nanometric bubbles. Moreover, helium bubbles tend to nucleate and grow at intrinsic or irradiation defects with sizeable free volumes, such as grain boundaries (GBs) and dislocations. While helium contributes to the safe use of fission reactor materials

in some cases, such as by protecting the integrity of the fuel rod cladding [12], it is harmful to structural material used in fusion reactors. A high density of helium bubbles on the GB can significantly weaken the GB cohesive strength and lead to a drop in the fracture stress, exacerbating the failure of RAFM steel via intergranular fracture. Therefore, it is essential to elucidate the underlying mechanism of helium-induced GB embrittlement and establish the relationship between the helium embrittlement susceptibility of GB and GB structure characteristics to explore possible ways to improve the resistance of RAFM steel against helium-induced GB embrittlement.

Few experiments have investigated the mechanical response of individual GBs to helium. For example, Miura et al. [13] investigated the effect of helium on the fracture properties of six different non-coincidence site lattice GBs of austenitic stainless steel by using micro-tensile tests combined with electron backscatter diffraction (EBSD) and focused ion beam (FIB) techniques. The results indicate that the segregation capacity of GBs to helium impurities plays an important role in GB helium embrittlement. However, there is no report on the results of GB micro-tensile tests of RAFM steels. Atomic scale simulation methods are convenient for investigating the mechanical behavior of different types of GBs under the influence of helium bubbles. Terentyev et al. [14] used uniaxial tensile simulations to study the effect of helium bubbles on the fracture processes of six different GBs with $\langle 110 \rangle$ as the tilt axis at 0 K in body-centered cubic (bcc) iron. The results indicate that the helium bubbles have a substantial effect on the fracture stress and strain of GBs and an intensive suppression on the slip related to plastic deformation. Moreover, our previous work [15] also investigated the effect of small helium-vacancy clusters on the tensile deformation of two types of symmetric tilt grain boundaries (STGBs) with $\langle 110 \rangle$ and $\langle 100 \rangle$ tilt axes at both 0 K and 300 K. The results indicated that the helium-vacancy clusters exert a significant suppressive effect on GB sliding and that the size effect of helium-vacancy clusters on GB sliding seems to be stronger than that of the He/V ratio. However, whether the helium embrittlement mechanism changes for different GBs remains unclear.

Moreover, in these previous simulation studies, a single helium bubble was created by removing Fe atoms from a spherical region and filling up the volume with helium atoms, which did not take into account the effect of GBs on helium segregation. In our recent work, we comprehensively investigated the effects of GB characteristic parameters on helium segregation, helium bubble nucleation and growth processes in bcc iron for high-energy neutron irradiation-related service environments [16]. The spatial distributions of helium bubbles in bubble-decorated bicrystal models were obtained via kinetic evolution at 600 K, and the helium concentration was set as 2000 appm. In this paper,

the uniaxial tensile simulations of 10 different clean GBs (4 GBs with $\langle 100 \rangle$ as the tilt axis and 6 GBs with $\langle 110 \rangle$ as the tilt axis) and their corresponding bubble-decorated GBs were performed at 600 K using molecular dynamics methods. The experimental characterization of ferritic steels has shown that several of the studied GBs were observed at concentrations higher than those of random GBs [17, 18]. The microscopic mechanism of helium-induced GB embrittlement at high temperatures was studied by comparing and analyzing the tensile processes of clean GBs and bubble-decorated GBs. The fracture strength and strain of bubble-decorated GBs were analyzed and correlated with the misorientation angle of GB to characterize the helium embrittlement susceptibilities of different GBs.

2 Simulation methods

In this work, the parallel molecular dynamics (MD) code LAMMPS [19, 20] was used to simulate the tensile processes of GBs in bcc iron with and without the presence of helium bubbles. The s–b and Fe–He many-body potential [21], along with the Fe–Fe potential of Ackland and Mendelev [22] and He–He potential of Aziz [23, 24], was selected to describe the interatomic interaction in the Fe–He system. Based on the potential set, the calculated properties are in good agreement with data from experimental and ab initio calculations demonstrated in previous works [25–29].

Based on the coincidence site lattice (CSL) theory, 10 types of STGBs that were observed at concentrations higher than those of random GBs [17, 18] were constructed via the bicrystal method. The GB is located at the interface of two perfect grains with different orientations. The detailed parameters of these GBs are listed in Table 1. To acquire the equilibrium GB structures of the bicrystal system, we sampled over 10,000 structures using rigid body translations. The displacement shift complete lattice was used to characterize the translational vector. The equilibrium structure was identified as the optimized lowest energy structure. Table 2 shows a comparison of the GB energy calculated in this paper with the results of DFT calculations [30–35] and other MD calculations [14, 36–38]. The majority of the GB energy values calculated in this work are consistent with other MD calculations but are slightly lower than the results obtained via DFT calculations. Details of the bicrystal method for the construction of GB structures can be found in Refs. [39–43]. In the Cartesian coordinate system of the simulation box, the tilt axis is aligned with the z-coordinate direction, and the normal direction of the GB is parallel to the y-coordinate direction. Figure 1 shows the side view of the supercells for 10 different STGBs. The structural units that make up each GB are marked in the figure.

Table 1 Detailed parameters of the studied STGBs

Tilt axis	Σ	GB plane	θ (deg)	N_{Fe}	L_x (nm)	L_y (nm)	L_z (nm)	D_{He} ($10^{26} m^{-3}$)	D_a (10^{-1} nm)
<110>	3	{111}	109.47	300,000	17.5	24.8	8.1	1.8	2.98
		{112}	70.53	302,400	17.3	25.2	8.1	1.9	4.07
	9	{114}	38.94	286,400	17.1	24.2	8.1	2.7	3.53
		{221}	141.06	300,160	17.0	25.5	8.1	4.5	3.06
	11	{113}	50.48	297,440	17.4	24.7	8.1	2.7	3.57
		{332}	129.52	285,120	17.0	24.1	8.1	2.5	3.94
<100>	5	{210}	53.13	299,488	17.9	24.5	8.0	2.4	3.58
		{310}	36.87	297,920	17.2	25.3	8.0	3.7	3.59
	13	{320}	67.38	296,072	17.5	24.7	8.0	2.4	3.82
		{510}	22.62	313,152	17.5	26.1	8.0	2.6	3.68

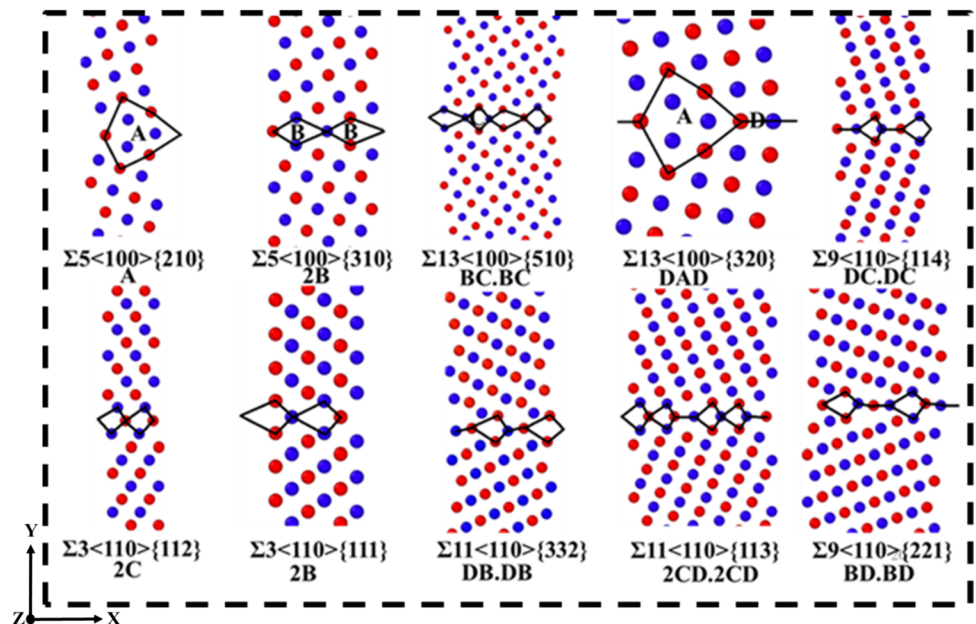
These parameters include tilt axis (<110> and <100>), coincidence index (Σ), GB plane index, misorientation angle (θ) in degrees, total number of iron atoms (N_{Fe}), initial supercell dimensions (L_x , L_y , and L_z) in nanometer, number density of GB helium bubbles (D_{He}) in m^{-3} and average diameter of GB helium bubbles (D_a) in nm

Table 2 Comparison between the GB energies (E_{GB} , in J/m^2) calculated in this work and in the literature

STGB type	E_{GB} (J/m^2)	MD calculations	DFT calculations
$\Sigma 3$ <110>{111}	1.308	1.308 ^a , 1.295 ^b	1.51 ^e , 1.52 ^f , 1.53 ^g
$\Sigma 3$ <110>{112}	0.260	0.260 ^a , 0.262 ^b	0.34 ^f , 0.43 ^g , 0.45 ^h
$\Sigma 5$ <100>{210}	1.113	1.113 ^a	1.61 ^g , 1.64 ^h
$\Sigma 5$ <100>{310}	1.008	1.008 ^a , 1.19 ^c	1.48 ^e , 1.49 ^f , 1.53 ^g
$\Sigma 9$ <110>{114}	1.286	1.286 ^{a,b} , 1.40 ^d	1.50 ^{e,h} , 1.38 ^g
$\Sigma 9$ <110>{221}	1.168	1.172 ^a , 1.167 ^b	1.66 ^h , 1.71 ⁱ , 1.62 ^j
$\Sigma 11$ <110>{113}	1.113	1.113 ^a , 1.03 ^c	1.45 ^h , 1.44 ^j
$\Sigma 11$ <110>{332}	1.019	1.02 ^a , 1.00 ^d	1.38 ^g , 1.47 ^h , 1.49 ⁱ
$\Sigma 13$ <100>{320}	1.108	1.108 ^a	1.53 ^h
$\Sigma 13$ <100>{510}	1.005	1.005 ^a	1.40 ^h

^aRef. [36]; ^bRef. [14]; ^cRef. [37]; ^dRef. [38]; ^eRef. [30]; ^fRef. [31]; ^gRef. [32]; ^hRef. [33]; ⁱRef. [34]; ^jRef. [35]

Fig. 1 (Color online) Schematic diagram of bcc iron bicrystals with STGBs located at the center. Iron atoms of each <100> or <110> layer are shown in a different color. The A, B, C and D notation refers to the different structural units that make up the GBs. The marks consisting of A, B, C and D below each GB refer to the structural units and its order that make up this GB



The He concentration in structural steels for the first wall of a fusion power plant can reach 1090 appm after 5 years [44] and 2000 appm after longer service time [10]. Thus, the initial helium concentration for our simulation was set as 2000 appm to study the GB mechanical properties at a high He concentration. Initially, all of the helium atoms were randomly distributed in the bicrystal model. A stable helium bubble distribution in the bicrystal model was obtained after 1.6 ns of MD evolution with the NPT ensemble under 600 K. Then, the bicrystal model with helium bubble distribution was used as the initial model for GB tensile simulation. The detailed process for building the initial models of bubble-decorated GBs and quantitative information on helium bubbles can be found in our previous work [16]. Owing to the high yield of helium, spallation neutron irradiation applications are widely used to test the properties of fusion reactor candidate materials. The distribution of high-density and small-sized helium bubbles on the GBs in the bubble-decorated GBs models (as shown in Fig. 2b) is consistent with the distribution of bubbles on the GBs in the spallation neutron irradiated RAFM steel specimens (as shown in Fig. 2c, d) presented in Refs. [45, 46].

The uniaxial tensile simulations for GBs with and without helium bubbles were performed under the same conditions. The tensile strain rate was set as 10^8 s^{-1} after comparison tests with 10^7 s^{-1} and 10^9 s^{-1} . The results showed that the deformation mechanism of GBs remains unchanged at different strain rates. Under the strain rate of 10^8 s^{-1} , relatively accurate fracture strength and strain values can be obtained while greatly saving computational resources. The direction

of the uniaxial tensile load is perpendicular to the GB plane. Periodic boundary conditions were applied along x and z directions. To avoid the interactions of boundary atoms in the y -direction, iron atoms more than 120 nm away from the GB plane were removed to create a vacuum layer, as shown in Fig. 2. In order to control the tensile strain, iron atoms located 115–120 nm from the GB plane were fixed. The strain was increased by moving both of the fixed layers, one along the positive y -direction and the other along the negative y -direction, and remapping the rest of the atom coordinates. Each strain step increased the strain by 0.01 percent, and this was followed by a 1.0 ps relaxation with the NVT ensemble under 600 K. This process was executed cyclically until the bicrystal model fractured. After the relaxation of each strain step, the strain and stress in the y -direction were recorded to analyze the tensile deformation process of the GB. The visualization and analysis of the atomic configurations were performed using the dislocation extraction analysis (DXA) and common neighbor analysis (CNA) as implemented in OVITO [47].

3 Results

The studied GBs can be classified into two categories based on the tensile behavior of clean GBs: (1) brittle GBs with no plastic deformation stage, including $\Sigma 3\{111\}$, $\Sigma 9\{114\}$, and $\Sigma 9\{221\}$ GB (hereafter, the notation of the tilt axis is omitted) and (2) ductile GBs with a plastic deformation stage. Ductile GBs have complex plastic deformation

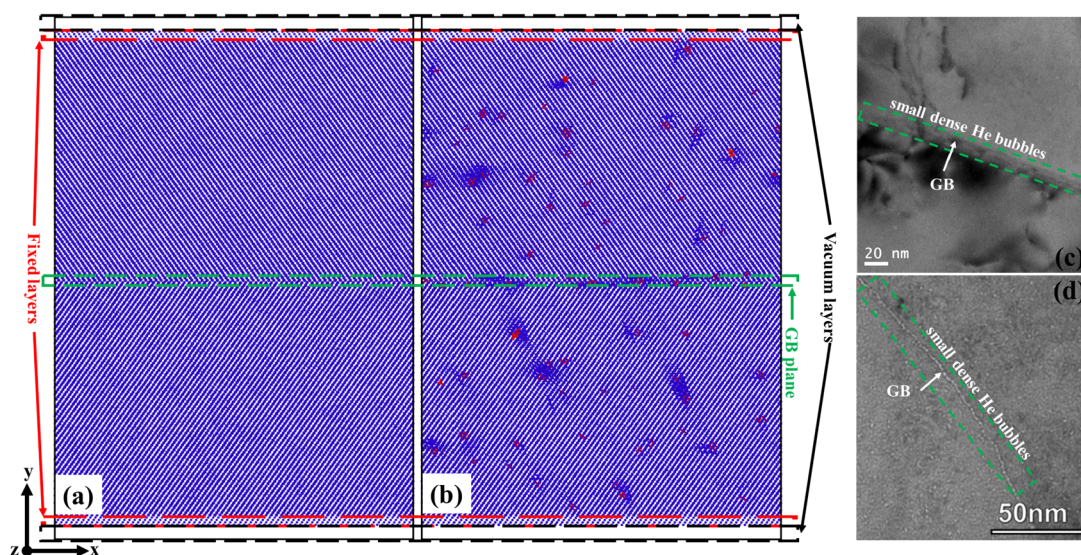


Fig. 2 (Color online) The uniaxial tensile model of **a** clean GB and **b** bubble-decorated GB, taking the $\Sigma 3\langle 110 \rangle\{112\}$ GB as an example. The red spheres in panel **(b)** represent helium atoms, and the blue spheres in both figures represent iron atoms. The vacuum layers, fixed

layers, and GB planes are indicated by black, red, and green rectangular boxes, respectively. Panels **(c)** and **(d)** [46] show a high-density distribution of small-scale helium bubbles at GBs in RAFM steel irradiated by spallation neutrons

mechanisms at high temperatures. The plastic deformation mechanisms observed in the current work can be classified into three categories: (1) Bain path phase transition with a lath structure, including $\Sigma 5\{210\}$, $\Sigma 5\{310\}$, $\Sigma 13\{320\}$ and $\Sigma 13\{510\}$ GB; (2) deformation twinning, which only occurs during the uniaxial tensile process of the twin boundary $\Sigma 3\{112\}$; (3) holonomic Bain/Burgers path phase transition, including $\Sigma 11\{113\}$ and $\Sigma 11\{332\}$ GB. In order to comprehensively study the plastic deformation behaviors of different clean GBs and elucidate the influence of helium bubbles on tensile deformation behavior, the tensile processes of GBs were investigated in detail by combining the stress–strain curves with an atomic configuration analysis.

The tensile deformation processes of $\Sigma 5\{210\}$, $\Sigma 5\{310\}$, $\Sigma 13\{320\}$, and $\Sigma 13\{510\}$ GBs via the first deformation mechanism, i.e., Bain path phase transition with a lath structure, were analyzed in Fig. 3. The results indicate that during uniaxial tensile simulations, the four clean GBs all underwent a plastic deformation stage in which the stress first dropped rapidly and then increased slowly. $\Sigma 5\{310\}$ GB was taken as an example to illustrate the deformation process from the atomic scale configuration perspective. Figure 3b–e shows the atomic scale configuration of the bicrystal at different stages during the tensile process. The stress and strain corresponding to each configuration are indicated

with stars in Fig. 3a. Figure 3b shows that the initial GB configuration remains intact at high temperatures. In the elastic stage, the stress increased linearly as the strain increased, and no phase transition initially occurred. Figure 3c shows that once the strain reached 7.28% and the corresponding stress reached 9.77 GPa, the GB region of the upper grain began to undergo a Bain path phase transition (bcc to fcc). Figure 3d shows that as the tensile strain increased, the phase transition region in the grain then began to expand to the fixed end in both upper and lower grains, and fcc lath grains were formed in the phase transition region. As the strain further increased, the phase transition region continued to expand, leading to an increased size of the lath grains. Figure 3e shows the largest phase transition region covering almost the entire grains. Soon after the strain reached a limit of 18.95%, cracks started to form at the GB plane. However, Fig. 3a shows that with the presence of helium bubbles, there was no plastic deformation stage in any of the four GBs. The elongation at the fractures decreased sharply, and the ultimate tensile strength also decreased. Figure 3f–i shows the atomic configurations of crack initiation in bubble-decorated $\Sigma 5\{210\}$, $\Sigma 5\{310\}$, $\Sigma 13\{320\}$, and $\Sigma 13\{510\}$ GB. As shown in the figure, no phase transition region appeared in the grains before the fracture of the bicrystals. When the applied stress surpassed a certain threshold, the dislocation

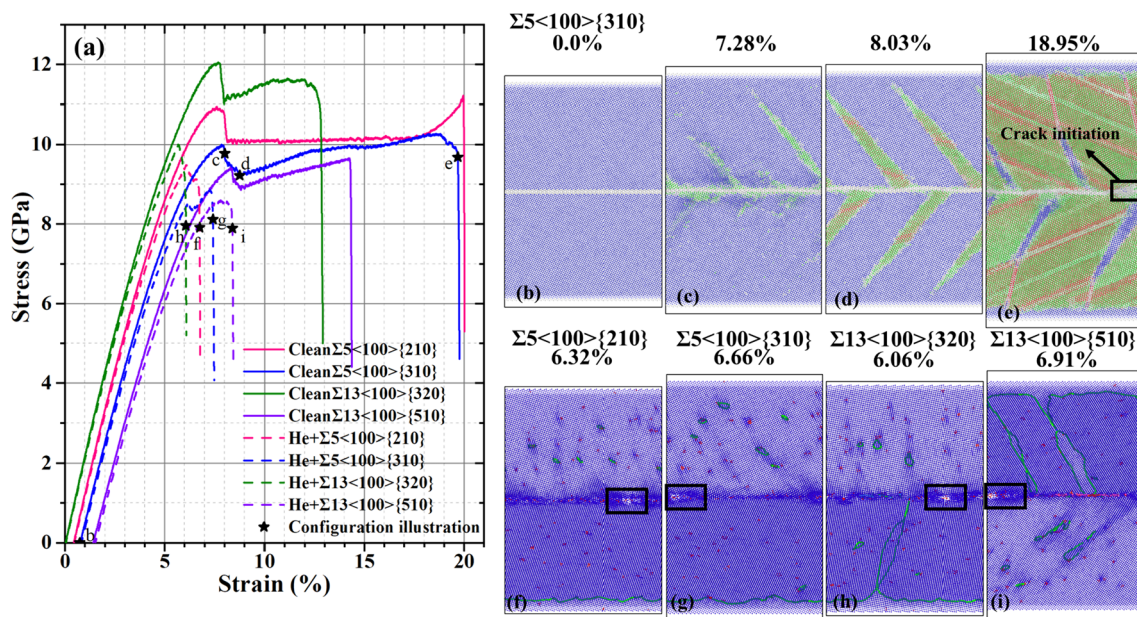


Fig. 3 (Color online) Stress–strain curves and atomic configurations of GBs with a Bain path phase transition and lath structure. **a** Stress–strain curves of $\Sigma 5\{210\}$, $\Sigma 5\{310\}$, $\Sigma 13\{320\}$, and $\Sigma 13\{510\}$ GBs with (dotted line) and without (solid line) helium bubbles. Panels **(b–e)** illustrate the atomic configurations of clean $\Sigma 5\{310\}$ GB at different deformation stages. The blue, green, red, and white spheres represent iron atoms with bcc, fcc, hcp, and other structures, respectively. Panels **(f–i)** illustrate the atomic configurations of the crack

initiation of bubble-decorated $\Sigma 5\{210\}$, $\Sigma 5\{310\}$, $\Sigma 13\{320\}$, and $\Sigma 13\{510\}$ GBs, respectively. Parts of the curves are horizontally translated for clarity. The blue spheres, red spheres, green lines, and pink lines represent iron atoms, helium atoms, $\frac{1}{2}\langle 111 \rangle$ dislocation/dislocation loops, and $\langle 100 \rangle$ dislocation/dislocation loops, respectively. The black rectangle indicates the regions where crack initiation occurred

loops nucleated around the helium bubbles in the bulk gradually grew and finally reached the fixed end of the bicrystal model, which absorbed part of the strain energy. Moreover, the helium bubbles on the GB reduced the bonding area of the boundary, which led to a drop in cohesive strength. In this case, the fracture stress was lower than the critical stress for the Bain path phase transition. This means that the existence of helium bubbles at the GB inhibited the channel of the Bain path phase transition, which led to the brittle rupture of the bicrystal at the GB.

The tensile deformation process of $\Sigma 3\{112\}$ GB via the second deformation mechanism, i.e., deformation twinning, was analyzed, as shown in Fig. 4. $\Sigma 3\{112\}$ GB is a unique twin GB, and the tensile direction along the $\langle 112 \rangle$ orientation leads to the activation of its twin system $\{112\} \langle 111 \rangle$ [48, 49]. In particular, Fig. 4a depicts the stress–strain curve of clean $\Sigma 3\{112\}$ GB, which shows that the tensile stress presented a fluctuating increase at the plastic deformation stage. During the uniaxial tensile test, atomic configurations of clean $\Sigma 3\{112\}$ GB were analyzed to explain this phenomenon, as shown in Fig. 4b–f. The stress and strain corresponding to each configuration

are indicated in Fig. 4a by stars. In contrast to other GBs, the initial $\Sigma 3\{112\}$ GB configuration is a narrow region consisting of two atomic layers, which reflects the peculiarity of $\Sigma 3\{112\}$ GB as a twin GB, as shown in Fig. 4b. The stress increased linearly with the strain in the elastic stage, and no phase transition occurred at this stage. Figure 4c, d shows that when the tensile strain reached 8.13% and the corresponding stress rose to 12.78 GPa, the GB plane started to slip along the $(1-21) [111]$ slip system to the fixed end and formed a set of deformation twins perpendicular to the original GB plane. The GB structures of the deformation twins were entirely consistent with the original twin boundary. Thereafter, the shape and size of the deformation twins were gradually optimized to be consistent under the action of applied stress, as shown in Fig. 4e. Figure 4h shows that the structures of these deformation twins closely match with those observed in RAFM [50, 51] and austenitic steels [13], as observed by TEM. However, the difference in critical stress for deformation twinning was relatively large, and this was mainly owing to the high strain rate in the MD simulation. During the twinning period, the tensile stress rose in a fluctuating manner. Figure 4f shows that with the

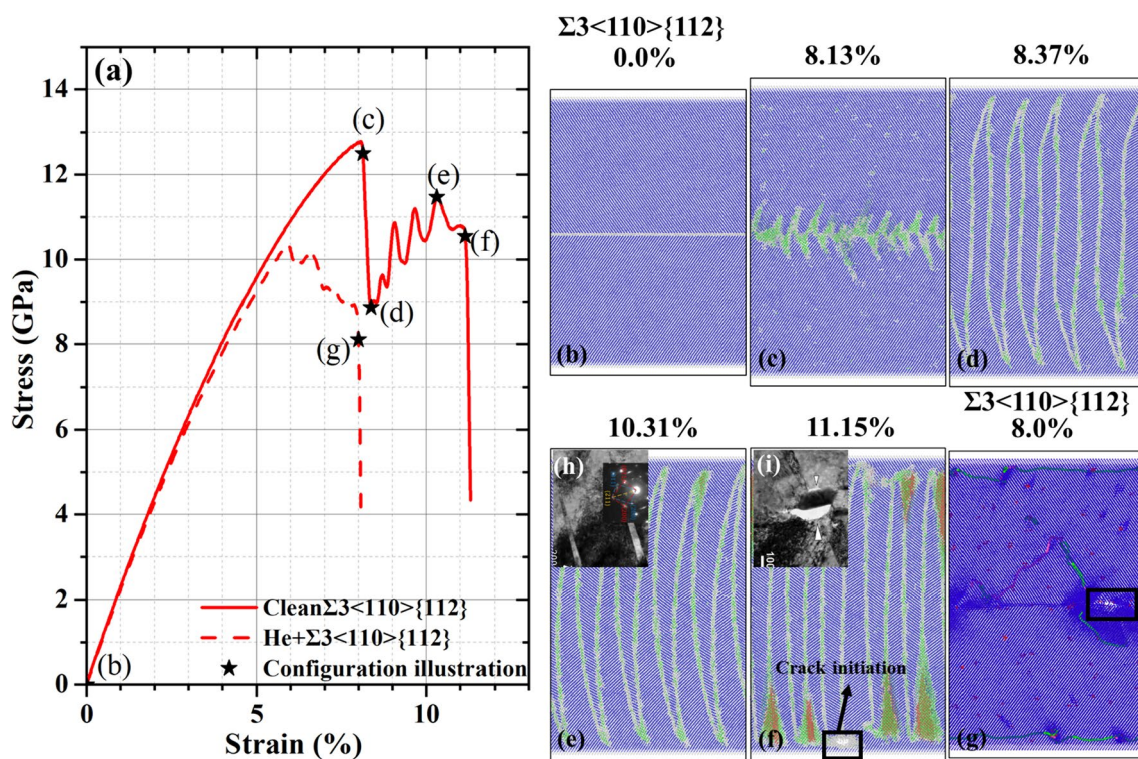


Fig. 4 (Color online) Stress–strain curves and atomic configurations of $\Sigma 3\{112\}$ GB with deformation twins. **a** Stress–strain curves of $\Sigma 3\{112\}$ GBs with (dotted line) and without (solid line) helium bubbles. Panels **(b–f)** illustrate the atomic configurations of clean $\Sigma 3\{112\}$ GB at different deformation stages. The blue, green, red, and white spheres represent iron atoms with bcc, fcc, hcp, and other structures, respectively. Panel **(g)** illustrates the atomic configura-

tion of the crack initiation of helium bubble-decorated $\Sigma 3\{112\}$ GB. The blue spheres, red spheres, green lines, and pink lines represent iron atoms, helium atoms, $\frac{1}{2} \langle 111 \rangle$ dislocation/dislocation loops, and $\langle 100 \rangle$ dislocation/dislocation loops, respectively. Panel **(h)** [51] shows the deformation twin structure observed during tensile tests under TEM. Panel **(i)** [51] shows the initiation of microcracks caused by deformation twins

further increase in strain, the high-stress state at the fixed end led to the formation of a Bain path phase transition region near the newly formed twin boundaries. Deformation twinning refined the newly formed grains, quickly hindering the expansion of the phase transition region. Eventually, the bicrystal fractures at the interface between the deformation twin boundary and the fixed end, which is consistent with the experimental finding that deformation twins can act as micro-crack initiators, as shown in Fig. 4i [51]. The stress–strain curve of the bubble-decorated $\Sigma 3\{112\}$ GB is shown with a dashed line in Fig. 4a. However, compared with clean $\Sigma 3\{112\}$ GB, the fracture strength and elongation of bubble-decorated GB are much lower. The fracture stress is lower than the critical stress for deformation twinning. Figure 4a shows that despite the process of deformation twinning having been inhibited, the twin boundary still retained some plasticity under the influence of helium bubbles. The atomic scale configuration showed that the plasticity derived from the relatively active dislocation evolution process at the crack tip, as shown in Fig. 4g.

Figure 5 shows the tensile deformation processes of $\Sigma 11\{113\}$ and $\Sigma 11\{332\}$ GBs via the third deformation mechanism, i.e., holonomic Bain/Burgers path phase transition. Figure 5a shows that both clean GBs underwent a plastic deformation stage with constant stress during the uniaxial tensile simulations. However, the atomic scale analysis

revealed that the two GBs had different phase transition mechanisms. Figure 5b–e shows the atomic scale configuration of the $\Sigma 11\{332\}$ GB with a Burgers path phase transition (bcc to hcp) at different stages during the tensile process. In Fig. 5a, a star indicates the corresponding stress and strain of each configuration. Figure 5g–j shows the atomic scale configuration of the $\Sigma 11\{113\}$ GB with a Bain path phase transition at different stages during the tensile process. The corresponding stress and strain of each configuration are also indicated in Fig. 5a by stars. As shown in Fig. 5b, g, the initial configurations of $\Sigma 11\{332\}$ and $\Sigma 11\{113\}$ GB were different. Some atoms at the $\Sigma 11\{332\}$ GB plane had atomic configurations similar to those of hcp crystals, which provided a large number of nucleation sites for Burgers path phase transitions. Nonetheless, the $\Sigma 11\{113\}$ GB does not have such a structure. As shown in Fig. 5c, h, when the strain increased to 7.64%/7.0%, the Burgers/Bain path phase transition began to progress steadily in the direction perpendicular to the original GB plane in $\Sigma 11\{332\}$ and $\Sigma 11\{113\}$ GB, respectively. As strain increased, atoms with the bcc structure on both sides of the GB continuously transformed into the hcp or fcc structure. Simultaneously, the bcc–hcp or bcc–fcc phase boundary began to move toward the fixed end of the bicrystal. During this period, the stress remained almost constant as the strain increased. Then, once the strain reached 10.86%/13.00%, the volume of the hcp/fcc region

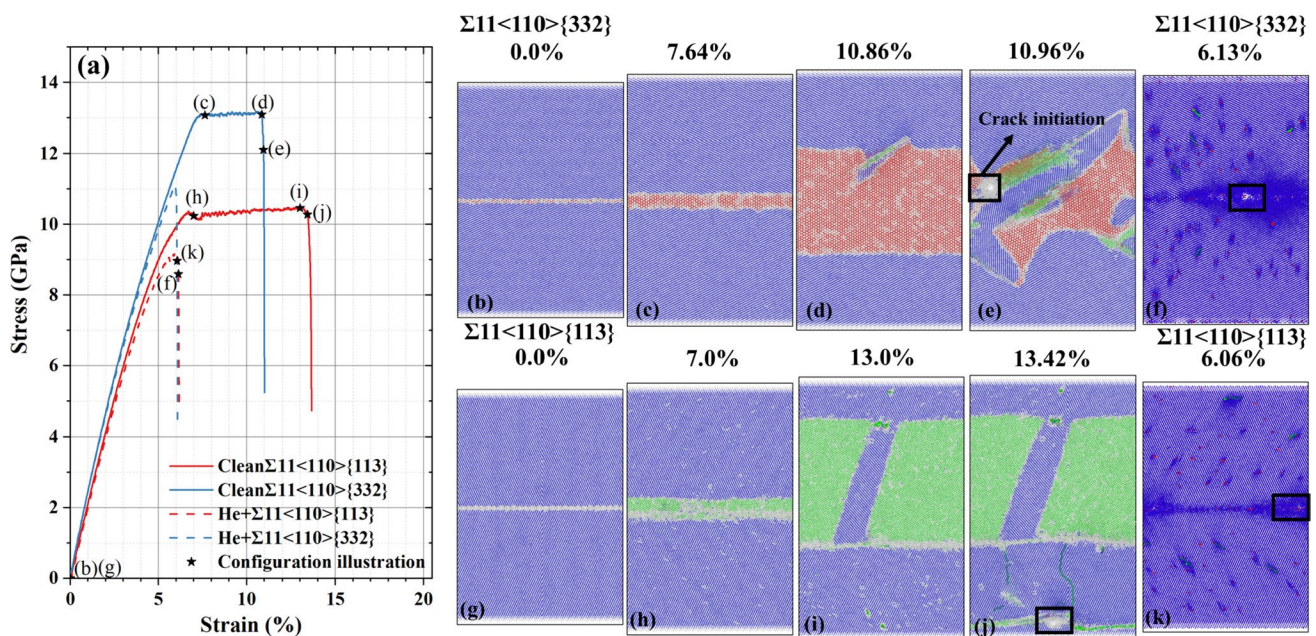


Fig. 5 (Color online) Stress–strain curves and atomic configurations of GBs with holonomic Bain/Burgers path phase transitions. **a** Stress–strain curves of $\Sigma 11\{113\}$ and $\Sigma 11\{332\}$ GBs with (dotted line) and without (solid line) helium bubbles. Panels (b–e) and (g–j) illustrate the atomic configurations of clean $\Sigma 11\{332\}$ and $\Sigma 11\{113\}$ GBs at different deformation stages, respectively. The

blue, red, green, and white spheres represent iron atoms with bcc, hcp, fcc, and other structures, respectively. Panels (f) and (k) illustrate the atomic configurations of the crack initiation of helium bubble-decorated GBs. The blue spheres, red spheres, and green lines represent iron atoms, helium atoms, and $1/2\langle 111 \rangle$ dislocation/dislocation loops, respectively

reached its maximum value for $\Sigma 11\{332\}$ and $\Sigma 11\{113\}$ GB, respectively, as shown in Fig. 5d, i.

Typically, the phase transition process continues until the bcc-hcp or bcc-fcc phase boundary reaches the fixed end at 0 K [15]. However, the phase boundary is unstable at high temperatures. Figure 5e shows that for $\Sigma 11\{332\}$ GB, a stacking fault slip occurred at the upper bcc-hcp phase boundary, resulting in the disruption of the Burgers path phase transition and the further destruction of the phase transition region. Likewise, Fig. 5j shows that for $\Sigma 11\{113\}$ GB, a series of dislocations were emitted from the lower bcc-fcc phase boundary and piled up at the fixed end of the lower grain, further resulting in the stress concentration and grain cracking at the lower fixed end. Also, under the effect of high temperature, at the beginning of the plastic deformation of the $\Sigma 11\{113\}$ GB, there was a stage where the stress briefly decreased. This stage was related to one dislocation emission at the GB in the initial stage. After the dislocation emission, the phase transition region was divided into two parts, as shown in Fig. 5i. Finally, when the strain reached 10.96%/13.42%, an initial crack formed in the slip band for $\Sigma 11\{332\}$ GB or at the lower fixed end for $\Sigma 11\{113\}$ GB, as shown in Fig. 5e, j.

In contrast, there was no phase transition during the tensile process of bubble-decorated $\Sigma 11\{332\}$ and $\Sigma 11\{113\}$ GB, and the initial crack presented at the grain boundary, as shown in Fig. 5f, k. Likewise, the fracture stress was lower than the critical stress for the Bain/Burgers path phase transitions, which led to the brittle fracture and a noticeable drop in the elongation.

Figure 6 shows the fracture processes of the three brittle GBs, namely, $\Sigma 3\{111\}$, $\Sigma 9\{114\}$, and $\Sigma 9\{221\}$, with and without helium bubbles. Figure 6a shows that the three clean GBs have similar stress–strain curves. Figure 6b–d presents the atomic configurations of three clean GBs just before fracture. The stress and strain corresponding to each configuration are indicated in Fig. 6a by stars. The configurations show that under the combined effects of high temperatures and stress, the GB regions of these bicrystals widened, and their original GB structure units were completely lost. In fact, the spatial distribution of atoms in the GB region became abnormally disordered [16]. The disorder of the GB structure hindered the aforementioned phase transition paths. Therefore, for clean GBs, the disorder of GB atoms is the fundamental cause of their brittle fractures. Figure 6e, f shows that the tensile behavior of bubble-decorated brittle

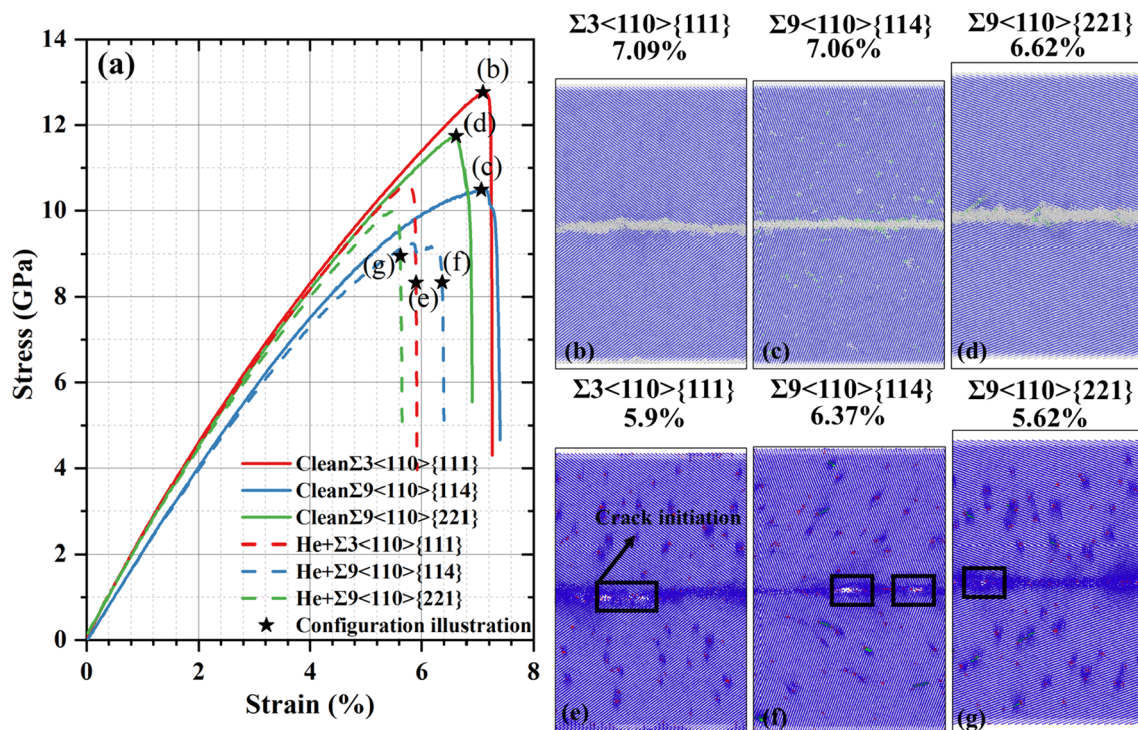


Fig. 6 (Color online) Stress–strain curves and atomic configurations of brittle GBs. **a** Stress–strain curves of $\Sigma 3\{111\}$, $\Sigma 9\{114\}$, and $\Sigma 9\{221\}$ GBs with (dotted line) and without (solid line) helium bubbles. Panels **(b–d)** illustrate the atomic configurations of clean $\Sigma 3\{111\}$, $\Sigma 9\{114\}$, and $\Sigma 9\{221\}$ GBs under ultimate tensile stress, respectively. The blue, green, and white spheres represent iron atoms

with bcc, fcc, and other structures, respectively. Panels **(e–g)** present the atomic configurations of the crack initiation of bubble-decorated $\Sigma 3\{111\}$, $\Sigma 9\{114\}$, and $\Sigma 9\{221\}$ GBs, respectively. The blue spheres, red spheres, and green lines represent iron atoms, helium atoms, and $1/2 \langle 111 \rangle$ dislocation/dislocation loops, respectively

GBs is similar to that of bubble-decorated ductile GB. Under the influence of helium bubbles, the fracture strength and elongation of GBs both decreased to varying degrees, as expected.

4 Discussion

To further analyze the role of the Bain path phase transition in the plastic deformation of ductile GBs, the orientation relationship in the Bain path phase transition from bcc to fcc was investigated, as shown in Fig. 7. Figure 7a–e shows the correspondence of the crystal planes and crystallographic directions in the bcc and fcc phases for $\Sigma 5\{210\}$, $\Sigma 5\{310\}$, $\Sigma 13\{320\}$, $\Sigma 13\{510\}$, and $\Sigma 11\{113\}$ GBs during the phase transition, respectively. In the phase transition process from the bcc structure to fcc structure, the $\langle 110 \rangle_\alpha$ direction in the bcc structure and the $\langle 121 \rangle_\gamma$ direction in the fcc structure were always parallel. In addition, the $\{110\}_\alpha$ plane in the bcc structure was always parallel to the $\{111\}_\gamma$ plane in the fcc structure. Figure 7f presents a schematic

diagram of the Bain path phase transition and shows that as long as a tensile deformation of about 40% occurs along the y-axis ($\langle 100 \rangle$ crystal direction), that is, as long as the lattice constant in the y-direction is elongated from the original a to $\sqrt{2}a$, the original bcc unit cell can be transformed into an fcc unit cell. The newly formed fcc unit cell has a lattice constant of $\sqrt{2}a$ and can therefore store higher strain energy than the original bcc unit cell with a as its lattice constant. For crystal planes, the $\{111\}_\gamma$ planes in the fcc lattice corresponded to the $\{110\}_\alpha$ planes in the bcc lattice. For the crystal orientation, the $\langle 112 \rangle_\gamma$ orientation in the fcc lattice corresponded to the $\langle 110 \rangle_\alpha$ orientation in the bcc lattice, and the $\langle 110 \rangle_\gamma$ orientation in the fcc lattice corresponded to the $\langle 111 \rangle_\alpha$ orientation in the bcc lattice. The correspondence of the crystal planes and crystallographic directions in the bcc and fcc phases during the GB phase transition are in agreement with the Bain path phase transition mechanism found in the bulk [52].

In order to investigate the susceptibility of different GBs to helium embrittlement, the relationship between the

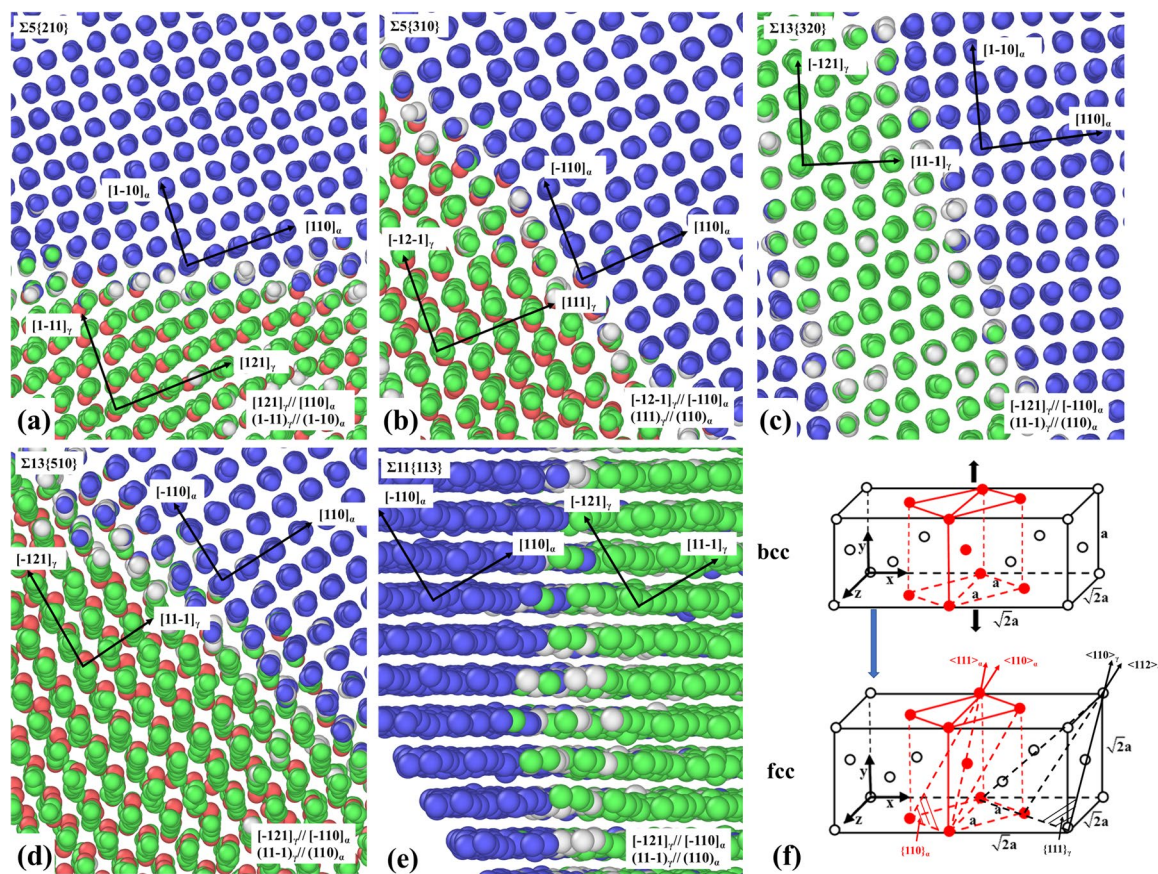


Fig. 7 (Color online) Schematic diagram of the orientation relationship in the Bain path phase transition from a bcc to an fcc lattice. **a** $\Sigma 5\{210\}$; **b** $\Sigma 5\{310\}$; **c** $\Sigma 13\{320\}$; **d** $\Sigma 13\{510\}$; **e** $\Sigma 11\{113\}$; **f** correspondence of the crystal planes and crystallographic directions

between the bcc and fcc phases. The blue, green, and yellow spheres represent iron atoms with bcc, fcc, and hcp structures, respectively, in panels (a–e). The solid red spheres represent the original bcc lattice before the phase transition in panel (f)

ultimate tensile (fracture) strength as well as the failure (fracture) strain and the misorientation angle under the influence of helium bubbles was analyzed, as shown in Fig. 8. For a comparative analysis, the ultimate tensile strength and failure strain for clean GBs are also included in Fig. 8a, b. First, the failure strain dropped under the influence of helium bubbles. Second, the ultimate tensile strength of individual GBs also decreased under the influence of helium bubbles, and this finding has been confirmed by the results of Ref. [13]. Previous experimentation has shown that the ultimate tensile strength of helium-containing GBs is related to the misorientation angle [13]. Our results in Fig. 8a further show that the ultimate tensile strength generally displayed an increasing trend as the misorientation angle increased. There is an excellent linear relationship between the ultimate tensile strength and the misorientation angle, especially for GBs with a $\langle 100 \rangle$ tilt axis. Compared with the tensile results of clean GBs, it was found that although helium bubbles reduce the ultimate tensile strength of each GB, they do not break the relationship between the ultimate tensile strength and misorientation angle.

Figure 8b shows the relationship between the failure strain and misorientation angle. The coherent twin boundary $\Sigma 3\{112\}$, with its low GB energy and sigma value, had a larger failure strain than the other bubble-decorated GBs, and it also had the lowest strain drop among the ductile GBs. Apart from the $\Sigma 3\{112\}$ GB, the fracture strain generally decreased as the misorientation angle increased. Compared with other bubble-decorated GBs, $\Sigma 3\{112\}$ GB displayed a high ultimate tensile strength while maintaining the largest

failure strain. Therefore, it is suggested that the distribution of $\Sigma 3\{112\}$ GBs in RAFM steel should be optimized by grain boundary engineering to improve their resistance to GB helium embrittlement, similar to the related improvement of resistance against intergranular damage in Refs. [8, 53–55].

5 Conclusion

In order to elucidate the microscopic mechanism of high temperature GB helium embrittlement and the susceptibility of different types of GBs to helium embrittlement in RAFM steel, we investigated the uniaxial tensile processes of 10 different clean GBs with two types of tilt axis (i.e., $\langle 110 \rangle$ and $\langle 100 \rangle$) as well as their corresponding bubble-decorated GBs in bcc iron at 600 K. The tensile behavior reveals that the studied GBs fall into two distinct categories: brittle and ductile. There are three different types of plastic deformation mechanisms in ductile GBs. The first type is a Bain path phase transition with a lath structure, which only occurs during the tensile process of GBs with $\langle 100 \rangle$ as the tilt axis. The second type is deformation twinning, which only occurs at the unique twin GB $\Sigma 3\{112\}$. The third type is a holonomic Bain/Burgers path phase transition, which occurs in some of the GBs with $\langle 110 \rangle$ as the tilt axis. The results of a structural analysis of the tensile process at the atomic scale imply that the plastic deformation mechanisms of almost all of the ductile GBs studied here are related to the Bain path phase

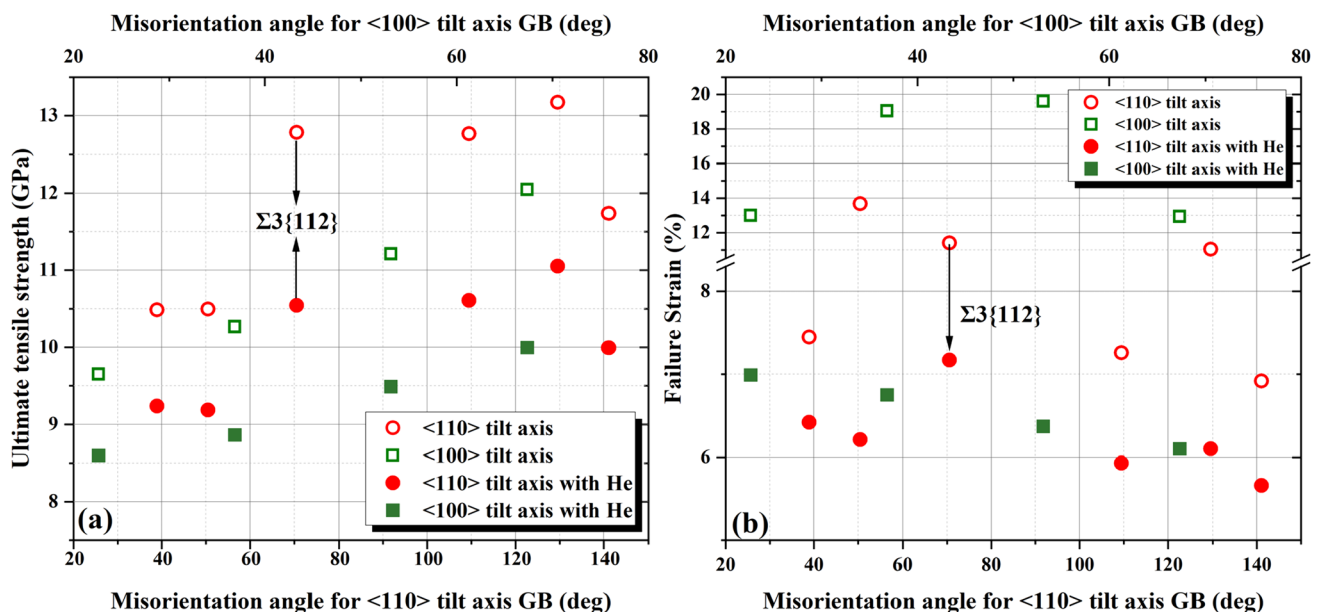


Fig. 8 (Color online) The relationship between **a** the ultimate tensile strength and **b** the failure strain and the misorientation angle for clean (hollow) and bubble-decorated (solid) GBs. The red circles and green squares refer to $\langle 110 \rangle$ and $\langle 100 \rangle$ tilt axis GBs, respectively

transition, which plays a vital role in the plastic deformation of the GBs. However, the presence of helium bubbles results in all GBs failing via brittle fracture and causes both the GB ultimate tensile strength and the failure strain to decrease. Helium bubbles significantly reduce the failure strain of ductile GBs by inhibiting the channel of plastic deformation. In the presence of helium bubbles, the ultimate tensile strength of GBs increases with the increase in the GB misorientation angle. The coherent twin GB $\Sigma\{112\}$ maintains the maximum failure strain and a relatively high ultimate tensile strength under the influence of helium bubbles.

Acknowledgements The numerical calculations in this paper were performed on the supercomputing system in the Supercomputing Center of the University of Science and Technology of China.

Author contributions All authors contributed to the study conception and design. Material preparation, data collection and analysis were performed by Lei Peng, Yong-Jie Sun and Jing-Yi Shi. The first draft of the manuscript was written by Yong-Jie Sun and Jing-Yi Shi, and all authors commented on previous versions of the manuscript. All authors read and approved the final manuscript.

Data availability The data that support the findings of this study are openly available in Science Data Bank at <https://cstr.cn/31253.11.sciencedb.j00186.00447> and <https://doi.org/10.57760/sciencedb.j00186.00447>.

Declarations

Conflict of interest The authors declare that they have no conflict of interests.

References

- Q.Y. Huang, X.Y. Wang, S.H. Sun et al., Development of reduced activation ferritic/martensitic steels in China. *J. Nucl. Mater.* **568**, 153887 (2022). <https://doi.org/10.1016/j.jnucmat.2022.153887>
- S.J. Zinkle, J.L. Boutard, D.T. Hoelzer et al., Development of next generation tempered and ODS reduced activation ferritic/martensitic steels for fusion energy applications. *Nucl. Fusion* **57**, 092005 (2017). <https://doi.org/10.1088/1741-4326/57/9/092005>
- L. Tan, L.L. Snead, Y. Katoh, Development of new generation reduced activation ferritic-martensitic steels for advanced fusion reactors. *J. Nucl. Mater.* **478**, 42–49 (2016). <https://doi.org/10.1016/j.jnucmat.2016.05.037>
- S.J. Zinkle, G.S. Was, Materials challenges in nuclear energy. *Acta Mater.* **61**, 735–758 (2013). <https://doi.org/10.1016/j.actamat.2012.11.004>
- Q. Huang, N. Baluc, Y. Dai et al., Recent progress of R&D activities on reduced activation ferritic/martensitic steels. *J. Nucl. Mater.* **442**, S2–S8 (2013). <https://doi.org/10.1016/j.jnucmat.2012.12.039>
- S.J. Zinkle, J.T. Busby, Structural materials for fission & fusion energy. *Mater. Today* **12**, 12–19 (2009). [https://doi.org/10.1016/S1369-7021\(09\)70294-9](https://doi.org/10.1016/S1369-7021(09)70294-9)
- R.J. Kurtz, A. Alamo, E. Lucon et al., Recent progress toward development of reduced activation ferritic/martensitic steels for fusion structural applications. *J. Nucl. Mater.* **386–388**, 411–417 (2009). <https://doi.org/10.1016/j.jnucmat.2008.12.323>
- L. Tan, K. Sridharan, T.R. Allen et al., Microstructure tailoring for property improvements by grain boundary engineering. *J. Nucl. Mater.* **374**, 270–280 (2008). <https://doi.org/10.1016/j.jnucmat.2007.08.015>
- T. Yamamoto, G.R. Odette, A fusion relevant data-driven engineering void swelling model for 9Cr tempered martensitic steels. *J. Nucl. Mater.* **576**, 154085 (2023). <https://doi.org/10.1016/j.jnucmat.2022.154085>
- Y. Dai, G.R. Odette, T. Yamamoto, The effects of helium in irradiated structural alloys. *Compr. Nucl. Mater.* **1**, 141–193 (2012). <https://doi.org/10.1016/b978-0-08-056033-5.00006-9>
- L.K. Mansur, A.F. Rowcliffe, R.K. Nanstad et al., Materials needs for fusion, generation IV fission reactors and spallation neutron sources - similarities and differences. *J. Nucl. Mater.* **329–333**, 166–172 (2004). <https://doi.org/10.1016/j.jnucmat.2004.04.016>
- F. Huang, Z. Zhu, H. Cao et al., Reliability analysis of helium pressure non-destructive testing method of the fuel rod. *Nucl. Tech. (in Chinese)* **46**, 070607 (2023). <https://doi.org/10.11889/j.0253-3219.2023.hjs.46.070607>
- T. Miura, K. Fujii, K. Fukuya, Micro-mechanical investigation for effects of helium on grain boundary fracture of austenitic stainless steel. *J. Nucl. Mater.* **457**, 279–290 (2015). <https://doi.org/10.1016/j.jnucmat.2014.11.062>
- D. Terentyev, X. He, Effect of Cr precipitates and He bubbles on the strength of $\langle 110 \rangle$ tilt grain boundaries in BCC Fe: an atomistic study. *Comput. Mater. Sci.* **50**, 925–933 (2011). <https://doi.org/10.1016/j.commatsci.2010.10.030>
- J.Y. Shi, L. Peng, M.Y. Ye et al., Molecular dynamics study: effects of He bubble and Cr precipitate on tensile deformation of grain boundaries in α -Fe. *IEEE Trans. Plasma Sci.* **45**, 289–293 (2017). <https://doi.org/10.1109/Tps.2016.2634778>
- Y.J. Sun, L. Peng, J.Y. Shi et al., Atomistic investigation on grain boundary effect on helium segregation and clustering in iron. *J. Nucl. Mater.* **569**, 153891 (2022). <https://doi.org/10.1016/j.jnucmat.2022.153891>
- H. Beladi, G.S. Rohrer, The distribution of grain boundary planes in interstitial free steel. *Metall. Mater. Trans. A* **44**, 115–124 (2013). <https://doi.org/10.1007/s11661-012-1393-0>
- H. Beladi, G.S. Rohrer, The relative grain boundary area and energy distributions in a ferritic steel determined from three-dimensional electron backscatter diffraction maps. *Acta Mater.* **61**, 1404–1412 (2013). <https://doi.org/10.1016/j.actamat.2012.11.017>
- A.P. Thompson, H.M. Aktulga, R. Berger et al., LAMMPS—a flexible simulation tool for particle-based materials modeling at the atomic, meso, and continuum scales. *Comput. Phys. Commun.* **271**, 108171 (2022). <https://doi.org/10.1016/j.cpc.2021.108171>
- S. Plimpton, Fast parallel algorithms for short-range molecular-dynamics. *J. Comput. Phys.* **117**, 1–19 (1995). <https://doi.org/10.1006/jcph.1995.1039>
- F. Gao, H.Q. Deng, H.L. Heinisch et al., A new Fe-He interatomic potential based on ab initio calculations in α -Fe. *J. Nucl. Mater.* **418**, 115–120 (2011). <https://doi.org/10.1016/j.jnucmat.2011.06.008>
- G.J. Ackland, M.I. Mendelev, D.J. Srolovitz et al., Development of an interatomic potential for phosphorus impurities in alpha-iron. *J. Phys. Condens. Matter* **16**, S2629–S2642 (2004). <https://doi.org/10.1088/0953-8984/16/27/003>
- R.A. Aziz, A.R. Janzen, M.R. Moldover, Ab-initio calculations for helium - a standard for transport property measurements. *Phys. Rev. Lett.* **74**, 1586–1589 (1995). <https://doi.org/10.1103/PhysRevLett.74.1586>
- R.A. Aziz, V.P.S. Nain, J.S. Carley et al., An accurate intermolecular potential for helium. *J. Chem. Phys.* **70**, 4330–4342 (1979). <https://doi.org/10.1063/1.438007>

25. M.A. Tschopp, F. Gao, K.N. Solanki, He–V cluster nucleation and growth in α -Fe grain boundaries. *Acta Mater.* **124**, 544–555 (2017). <https://doi.org/10.1016/j.actamat.2016.11.027>
26. L. Zhang, C.C. Fu, E. Hayward et al., Properties of He clustering in alpha-Fe grain boundaries. *J. Nucl. Mater.* **459**, 247–258 (2015). <https://doi.org/10.1016/j.jnucmat.2015.01.008>
27. L. Yang, F. Gao, R.J. Kurtz et al., Effects of local structure on helium bubble growth in bulk and at grain boundaries of bcc iron: A molecular dynamics study. *Acta Mater.* **97**, 86–93 (2015). <https://doi.org/10.1016/j.actamat.2015.06.055>
28. L. Yang, F. Gao, R.J. Kurtz et al., Atomistic simulations of helium clustering and grain boundary reconstruction in alpha-iron. *Acta Mater.* **82**, 275–286 (2015). <https://doi.org/10.1016/j.actamat.2014.09.015>
29. H.Q. Deng, W.Y. Hu, F. Gao et al., Diffusion of small He clusters in bulk and grain boundaries in α -Fe. *J. Nucl. Mater.* **442**, S667–S673 (2013). <https://doi.org/10.1016/j.jnucmat.2013.02.063>
30. L. Zhang, C.C. Fu, G.H. Lu, Energetic landscape and diffusion of He in α -Fe grain boundaries from first principles. *Phys. Rev. B* **87**, 134107 (2013). <https://doi.org/10.1103/PhysRevB.87.134107>
31. N. Gao, C.C. Fu, M. Samaras et al., Multiscale modelling of bicrystal grain boundaries in bcc iron. *J. Nucl. Mater.* **385**, 262–267 (2009). <https://doi.org/10.1016/j.jnucmat.2008.12.016>
32. J. Xu, Y. Jiang, L.T. Yang et al., Assessment of the CSL and SU models for bcc-Fe grain boundaries from first principles. *Comput. Mater. Sci.* **122**, 22–29 (2016). <https://doi.org/10.1016/j.commat.2016.05.009>
33. J.L. Wang, G.K.H. Madsen, R. Drautz, Grain boundaries in bcc-Fe: a density-functional theory and tight-binding study. *Modelling Simul. Mater. Sci. Eng.* **26**, 025008 (2018). <https://doi.org/10.1088/1361-651X/aa9f81>
34. S.K. Bhattacharya, S. Tanaka, Y. Shiihara et al., Ab initio perspective of the $\langle 110 \rangle$ symmetrical tilt grain boundaries in bcc Fe: application of local energy and local stress. *J. Mater. Sci.* **49**, 3980–3995 (2014). <https://doi.org/10.1007/s10853-014-8038-1>
35. T.D. Pham, T.Q. Nguyen, T. Terai et al., Segregation of carbon in α -Fe symmetrical tilt grain boundaries studied by first-principles based interatomic potential. *Mater. Trans.* **62**, 1057–1063 (2021). <https://doi.org/10.2320/matertrans.MT-M2021054>
36. M.A. Tschopp, F. Gao, L. Yang et al., Binding energetics of substitutional and interstitial helium and di-helium defects with grain boundary structure in α -Fe. *J. Appl. Phys.* **115**, 033503 (2014). <https://doi.org/10.1063/1.4861719>
37. T. Suzudo, T. Tsuru, M. Yamaguchi et al., An atomistic modeling of He bubble stability at grain boundaries in α -Fe. *J. Nucl. Mater.* **442**, S655–S659 (2013). <https://doi.org/10.1016/j.jnucmat.2013.03.082>
38. R.J. Kurtz, H.L. Heinisch, The effects of grain boundary structure on binding of He in Fe. *J. Nucl. Mater.* **329–333**, 1199–1203 (2004). <https://doi.org/10.1016/j.jnucmat.2004.04.262>
39. M.A. Tschopp, K.N. Solanki, F. Gao et al., Probing grain boundary sink strength at the nanoscale: Energetics and length scales of vacancy and interstitial absorption by grain boundaries in α -Fe. *Phys. Rev. B* **85**, 064108 (2012). <https://doi.org/10.1103/PhysRevB.85.064108>
40. K.N. Solanki, M.A. Tschopp, M.A. Bhatia et al., Atomistic investigation of the role of grain boundary structure on hydrogen segregation and embrittlement in α -Fe. *Metall. Mater. Trans. A* **44**, 1365–1375 (2013). <https://doi.org/10.1007/s11661-012-1430-z>
41. G.J. Tucker, M.A. Tschopp, D.L. McDowell, Evolution of structure and free volume in symmetric tilt grain boundaries during dislocation nucleation. *Acta Mater.* **58**, 6464–6473 (2010). <https://doi.org/10.1016/j.actamat.2010.08.008>
42. M.A. Tschopp, G.J. Tucker, D.L. McDowell, Structure and free volume of $\langle 110 \rangle$ symmetric tilt grain boundaries with the E structural unit. *Acta Mater.* **55**, 3959–3969 (2007). <https://doi.org/10.1016/j.actamat.2007.03.012>
43. M.A. Tschopp, D.L. McDowell, Structures and energies of Sigma 3 asymmetric tilt grain boundaries in copper and aluminium. *Philos. Mag.* **87**, 3147–3173 (2007). <https://doi.org/10.1080/14786430701255895>
44. M.R. Gilbert, J.C. Sublet, Neutron-induced transmutation effects in W and W-alloys in a fusion environment. *Nucl. Fusion* **51**, 043005 (2011). <https://doi.org/10.1088/0029-5515/51/4/043005>
45. Y. Dai, J. Henry, Z. Tong et al., Neutron/proton irradiation and He effects on the microstructure and mechanical properties of ferritic/martensitic steels T91 and EM10. *J. Nucl. Mater.* **415**, 306–310 (2011). <https://doi.org/10.1016/j.jnucmat.2011.04.029>
46. K. Wang, C.M. Parish, K.G. Field et al., Segregation behavior and phase instability of Eurofer97 after neutron irradiation to 72 dpa. *J. Nucl. Mater.* **547**, 152834 (2021). <https://doi.org/10.1016/j.jnucmat.2021.152834>
47. A. Stukowski, Visualization and analysis of atomistic simulation data with OVITO—the open visualization tool. *Modelling Simul. Mater. Sci. Eng.* **18**, 015012 (2010). <https://doi.org/10.1088/0965-0393/18/1/015012>
48. X. Wang, J.W. Wang, Y. He et al., Unstable twin in body-centered cubic tungsten nanocrystals. *Nat. Commun.* **11**, 2497 (2020). <https://doi.org/10.1038/s41467-020-16349-8>
49. B.B. Jiang, A.D. Tu, H. Wang et al., Direct observation of deformation twinning under stress gradient in body-centered cubic metals. *Acta Mater.* **155**, 56–68 (2018). <https://doi.org/10.1016/j.actamat.2018.05.061>
50. K. Wang, Y. Dai, P. Spätig, Microstructure and fracture behavior of F82H steel under different irradiation and tensile test conditions. *J. Nucl. Mater.* **468**, 246–254 (2016). <https://doi.org/10.1016/j.jnucmat.2015.09.031>
51. K. Wang, Y. Dai, P. Spätig, Deformation twinning in irradiated ferritic/martensitic steels. *J. Nucl. Mater.* **501**, 336–346 (2018). <https://doi.org/10.1016/j.jnucmat.2018.01.057>
52. D.M. Clatterbuck, D.C. Chrzan, J.W. Morris, The ideal strength of iron in tension and shear. *Acta Mater.* **51**, 2271–2283 (2003). [https://doi.org/10.1016/S1359-6454\(03\)00033-8](https://doi.org/10.1016/S1359-6454(03)00033-8)
53. G. Gupta, G.S. Was, B. Alexandreanu, Grain boundary engineering of ferritic-martensitic alloy T91. *Metall. Mater. Trans. A* **35**, 717–719 (2004). <https://doi.org/10.1007/s11661-004-0382-3>
54. G. Gupta, P. Ampornrat, X. Ren et al., Role of grain boundary engineering in the SCC behavior of ferritic–martensitic alloy HT-9. *J. Nucl. Mater.* **361**, 160–173 (2007). <https://doi.org/10.1016/j.jnucmat.2006.12.006>
55. K. Hirayama, Y. Yoshii, Y. Morizono et al., Grain boundary engineering of 10% Cr ferritic-martensitic steel SUH3. *ISIJ Int.* **55**, 1973–1979 (2015). <https://doi.org/10.2355/isijinternational.ISIJNT-2015-057>

Springer Nature or its licensor (e.g. a society or other partner) holds exclusive rights to this article under a publishing agreement with the author(s) or other rightsholder(s); author self-archiving of the accepted manuscript version of this article is solely governed by the terms of such publishing agreement and applicable law.